Dinitrogen bonding induced metal-semiconductor transition leading to ultrastiffening in boron subnitride

Tengfei Xu,[1] Zhiyang Zheng,[1] Dominik Legut,[2,3] and Ruifeng Zhang[1,*]

[1]*School of Materials Science and Engineering, and Center for Integrated Computational Engineering (International Research Institute for Multidisciplinary Science) and Key Laboratory of High-Temperature Structural Materials & Coatings Technology (Ministry of Industry and Information Technology), Beihang University, Beijing 100191, People's Republic of China*
[2]*IT4Innovations, VSB-Technical University of Ostrava, CZ-708 00 Ostrava, Czech Republic*
[3]*Department of Condensed Matter Physics, Faculty of Mathematics and Physics, Charles University, CZ-121 16 Prague, Czech Republic*

(Received 18 January 2023; revised 13 May 2023; accepted 27 October 2023; published 13 November 2023)

Extreme environments enable the discovery of atypical phases with enhanced properties and their transition mechanisms. Boron subnitride is a promising alternative to boron carbide/suboxide; however, its development is severely hampered by its long-standing unresolved crystal structure. Herein, by analyzing the pressure-dependent stabilities of the B-N system and scrutinizing several candidates against the available experimental results, the experimentally synthesized boron subnitride is identified as α-B_6O-like $R\bar{3}m$ B_6N, whose observed unique metallicity originates from the electron deficiency caused by the sp^2-like hybridization of the N atoms that leaves nonbonding lone pairs lying in the $2p_z$ orbitals. We further unveil that the electron-deficient $R\bar{3}m$ B_6N undergoes an isopointal metal-semiconductor transition at 120 GPa, dominated by the unique local orbital population coupling between different homonuclear bonds. Here, breakage of the lone pairs resulting from the dinitrogen bonding compensates for the unoccupied bonding states of intericosahedra B-B bonds, thus converting it into the electron-precise $B_{12}^{2-}(\text{N-N})^{2+}$. The strong N-N bond imparts $R\bar{3}m$ B_6N the highest shear modulus among B_{12}-based compounds (almost twice that of B_6O) and serves as the main load-bearing unit resisting large plastic strain to produce superior strength. These findings substantially deepen our fundamental understanding of icosahedral boron-rich solids, and the underlying effect may contribute to fully grasping the changes in oxidation state and bonding pattern under high pressures.

DOI: 10.1103/PhysRevB.108.L180103

Boron exhibits structural complexity, electron deficiency, and an unusual bonding situation, giving rise to many boron-rich compounds [1–4]. In particular, strong icosahedral boron-rich solids hosting light elements such as boron carbides [5–9] and boron suboxide [10–12] have garnered theoretical and experimental attention because of their fascinating physical and chemical properties as well as their numerous potential applications [13–17]. Despite the successful synthesis of boron subnitride at high pressure [18,19], the long-standing disagreement about its actual crystal structure has hindered further development [18,20,21], leaving inconclusive issues regarding its ground-state properties, e.g., the origin of the observed metallic conductivity [19,22], and its effects on the mechanical properties. Previous studies have shown that the chemistry of boron-rich compounds with homonuclear bonds (e.g., boron clusters) [23–25], and binary nitrides containing polynitrogen species [26–28] can be remarkedly enriched under pressure, resulting in promising exotic phases [29]. It is therefore intriguing to explore the high-pressure behavior of boron subnitride, where the effects of these two components may be coupled with each other and further magnified under a compressed state, thus allowing not only geometry alterations through potential phase transitions, but also drastic changes in chemical bonding and physical properties via huge electronic modifications.

The debate on the realistic crystal structure of boron subnitride has initiated three different candidates with α-rhombohedral-boron-like structures: two individual line compounds [B_{12}(NN)] [18], i.e., B_6N and B_{12}(N-B-N) [21], i.e., $B_{13}N_2$] and one solid solution ([B_{12}(NN)]$_{0.33}$[B_{12}(N-B-N)]$_{0.67}$ [30], i.e., $B_{38}N_6$). Recently, by comparing the high-pressure formation enthalpy of the above three materials, Ektarawong *et al.* [20] found that $B_{38}N_6$ is more thermodynamically favorable than B_6N and $B_{13}N_2$ and thus should represent the synthesized boron subnitride. However, the realistic crystal structure cannot be verified based on the very limited structures under consideration since high pressure (i.e., the experimental pressure of ~7.5 GPa) usually produces various polytypes that serve as the competitors through structural evolution. Besides the stability, the crystallographic information [i.e., x-ray diffraction (XRD) pattern] and intrinsic electronic property (i.e., metallic conductivity) reflected by the experimental characterizations [18,19] should be consistent with the candidate structures, yet all these factors were largely neglected in previous studies.

Given that borides formed from P (B_6P) [31,32] and As (B_6As) [32,33]—which have the same valence electron arrangement ($2s^2\,2p^3$) as N—are semiconductors, it is reasonable to believe that the conductivity of boron subnitride

---

[*] zrf@buaa.edu.cn

is highly determined by the local bonding patterns associated with N atoms. Consequently, these characteristics are expected to play a dominant role in its mechanical behavior. Further considering the complex high-pressure phase transition paths as discovered in elemental boron [23] and boron suboxide [34,35], and even more generally the modification due to pressure sensitivity of local structural characters (e.g., the pressure-induced metallization of α-B_{12} caused by the shortening of the three-center bonds [36,37], and the high-pressure mechanical softening of B_4C dominated by the bending of the three-atom chain [38,39]), it is natural to wonder whether the localized (i.e., N-related and B-B homonuclear bonds) orbital patterns of boron subnitride could be substantially altered under pressure, leading to the potential phase transition that impacts the deformation mechanism and brings about novel mechanical properties. This phenomenon would be encouraging since the widely used B_{12}-based compounds, e.g., boron carbide and boron suboxide, find very limited application under extreme environments due to their structural instability [38,39] and intrinsic low stiffness [11,40].

In this Letter, by evaluating the pressure-dependent thermodynamic stability of the B-N system, we show that both the proposed B_6N, $B_{13}N_2$ and $B_{38}N_6$ are metastable, in which $R\bar{3}m$ B_6N represents the actual crystal structure of the experimental phase. At 120 GPa, the electron-deficient $R\bar{3}m$ B_6N transforms into an electron-precise semiconductor because of the orbital repopulation associated with the N-N and the intericosahedra B-B bonds. This N-N bond endows $R\bar{3}m$ B_6N with extraordinarily high stiffness and plays a dominant role in bearing large shear loadings, resulting in effective strengthening at high pressures. Similar behaviors are also observed in *Cmcm* B_6N, a nanotwinned phase of $R\bar{3}m$ B_6N with β-B_6O-like crystal structure.

Since high pressure enables the creation of new materials through phase transition [29], the identification of experimentally synthesized boron subnitride first requires a comprehensive thermodynamic assessment on the B-N system at both normal and experimental pressure. Our extensive structure search based on evolutionary algorithms successfully predicted a unique *Pmna* B_6N phase and reproduced several boron subnitride polymorphs [41] (see Fig. S1 and Table S1 in the Supplemental Material [42] for details of crystal structure; see also Refs. [4,18,29,43–71]). The convex hulls show that both $R\bar{3}m$ B_6N, $R\bar{3}m$ $B_{13}N_2$ and $B_{38}N_6$ are metastable regardless of zero or high pressures, whereas only *Cmca* B_6N is the stable phase lying in the convex hull [Fig. 1(a)]. However, the serious mismatch between the simulated XRD pattern of *Cmca* B_6N with the experimental data excludes it as the boron subnitride candidate, and other B_6N structures as well as $C2/m$ $B_{13}N_2$ can also be ruled out for the same reason [Fig. 2(a)]. For $R\bar{3}m$ $B_{13}N_2$ and $B_{38}N_6$, noticeable deviations of the main diffraction peaks can be detected in the $1/d$ spacing range of 0.2–0.5 [Fig. 2(b)], strongly challenging the rationality of these two structures. Besides, the semiconductor feature of $B_{38}N_6$ (Fig. S2(a) [42]) and the dynamic instability of $R\bar{3}m$ $B_{13}N_2$ (Figs. S3(a) and S3(c) [42]) disqualify them from being the experimental phase. In contrast, $R\bar{3}m$ B_6N reproduces not only the experimental XRD pattern perfectly [Fig. 2(b)], but its metallic feature (Fig. S2(b) [42]), phonon (Figs. S3(b) and S3(d) [42]) and mechanical stabilities (single-crystal constants [58,72] listed in Table S2 [42]) were corroborated. We further provide a possible explanation for the formation of $R\bar{3}m$ B_6N from the kinetic aspects by considering the starting material and the reaction process [18,68] (see Supplemental Material S4, for details [42]). This formation mechanism is indirectly supported by the kinetics revealed in the synthesis of $R\bar{3}m$ B_6O [70,71], in view of their significant structural packing similarity to the "supericosahedron" of β-B [4,69]. Hence, $R\bar{3}m$ B_6N represents the most likely crystal structure of the experimentally synthesized boron subnitride, which is consistent with the initial speculation of Hubert *et al.* [18].

To further probe the stability and the potential phase transition of $R\bar{3}m$ B_6N under extreme conditions, the pressure-dependent enthalpy relations of different B_6N polymorphs were calculated. As shown in Fig. 1(b), a potential phase transition can be observed between the *Pmna* and *Imma* phases, while they are not related to $R\bar{3}m$ B_6N. It is an interesting finding that *Cmcm* B_6N is slightly more stable than $R\bar{3}m$ B_6N, with a formation enthalpy at ambient pressure of only ~2.1 meV lower than the latter, which can be seen as a 1×1 zigzag nanotwinned phase of $R\bar{3}m$ B_6N. These findings show a high similarity to the relations between boron suboxide $R\bar{3}m$ B_6O and its nanotwinned *Cmcm* B_6O that both have been successfully synthesized [34,73,74]. The above results and the verified lattice and mechanical stabilities (Fig. S4, and Tables S2 and S3 [42]) indicate that once $R\bar{3}m$ B_6N and *Cmcm* B_6N are synthesized, they can be stable to at least 200 GPa without any structural phase transition. However, an unexpected nonlinear decrease in the volume changes of $R\bar{3}m$ B_6N emerges, corresponding to the turning point of its c/a variation at 120 GPa [Fig. 1(d)]. The key bond length changes [Fig. 1(c)] show that homonuclear N-N and B_p-B_p bond lengths are substantially reduced by ~51% and ~13%, respectively, whereas the heteronuclear B_e-N bond varies negligibly (~3%), which follows the general propensity of increased homogeneity under pressure indicated by the diatomic Hückel model [29]. Particularly, the N-N distance (1.61 Å) becomes closer to the typical N-N single bond (1.45 Å) [75], which may indicate a nonbonding to single bonding state transition. Similar structural changes are also observed in *Cmcm* B_6N (Fig. S5 [42]). These behaviors are plausibly a sign of isopointal phase transition since the symmetry (the space group and Wyckoff positions) of $R\bar{3}m$ B_6N and *Cmcm* B_6N remains unchanged, and the formation of the N-N bond along with the increased B_p-B_p interactions may be the underlying driving mechanism for such electronic transition.

To verify the above picture, we first calculated the electron localization function (ELF) of $R\bar{3}m$ B_6N and *Cmcm* B_6N at zero and high pressures (Figs. 3(a) and S6(a) [42]). The ELF map clearly shows the appearance of covalent bonding characters between N sites at 120 GPa (red rectangles), which is also evident by their valence charge density difference (VCDD) variations, where the charge accumulation area can be observed in the center of the N-N bond at 120 GPa (black rectangles). Further increasing the pressure to 200 GPa, this N-N bonding situation remains unchanged. Atom-resolved band structures unveil that the metallic nature of these two structures at ambient pressure mainly involves B_p (or B_B)

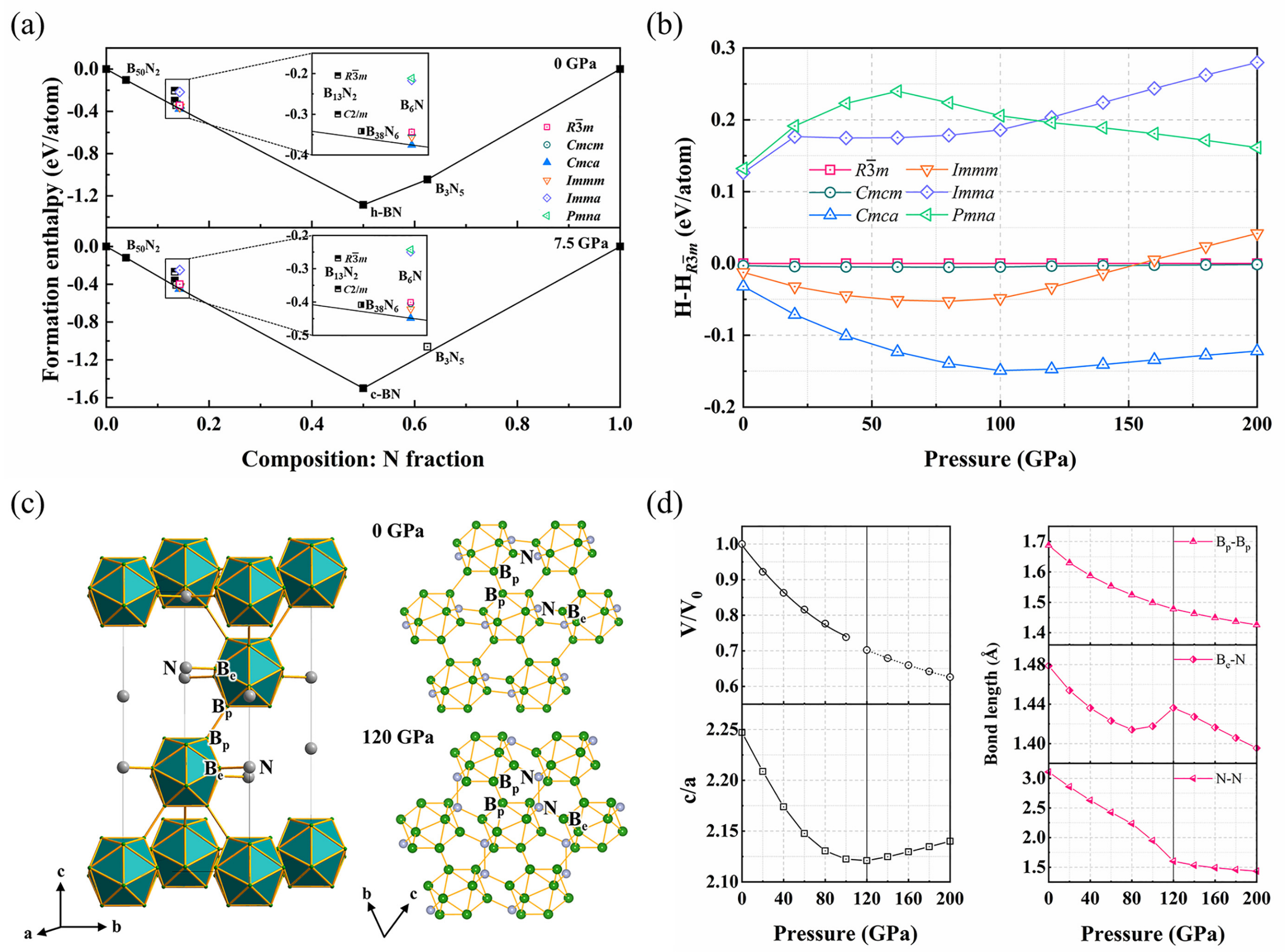

FIG. 1. (a) Convex hull diagram for B-N system at zero and experimental pressures. Only stoichiometries with formation enthalpies lying on convex hull (solid symbols) and the potential boron subnitride candidates (insets) are presented. (b) Relative enthalpy vs pressure for different B_6N phases. (c) The crystal structure of $R\bar{3}m$ B_6N (left) and characterization of structural changes at 0 and 120 GPa (right). (d) Volume, lattice parameters and key bond lengths of $R\bar{3}m$ B_6N in relation to pressure.

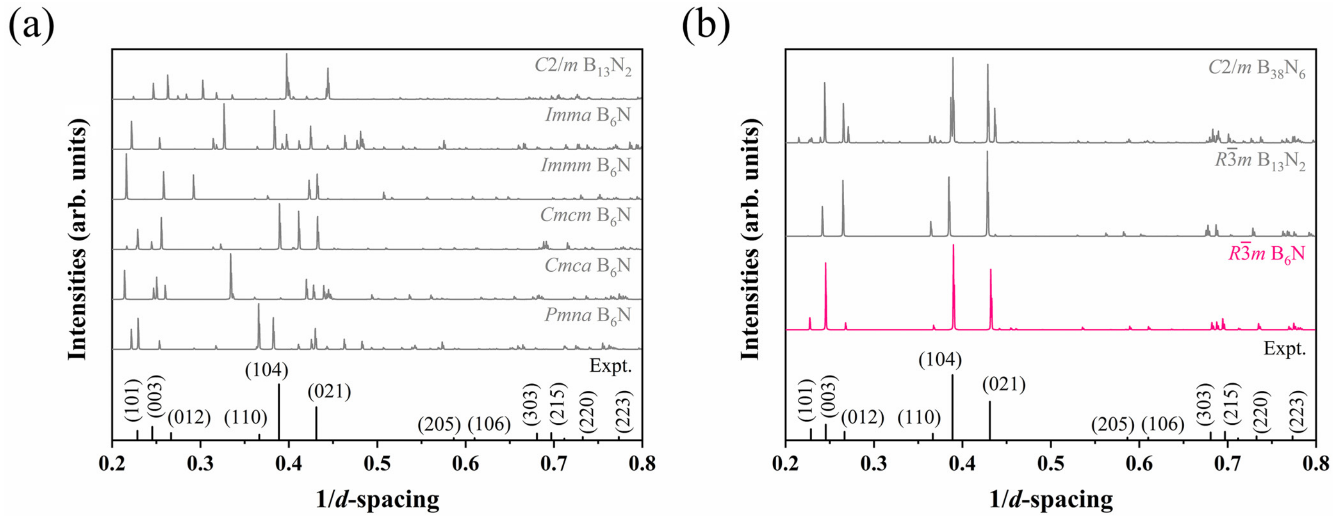

FIG. 2. (a), (b) Simulated XRD patterns of several boron subnitride and the experimental pattern reproduced from Ref. [18].

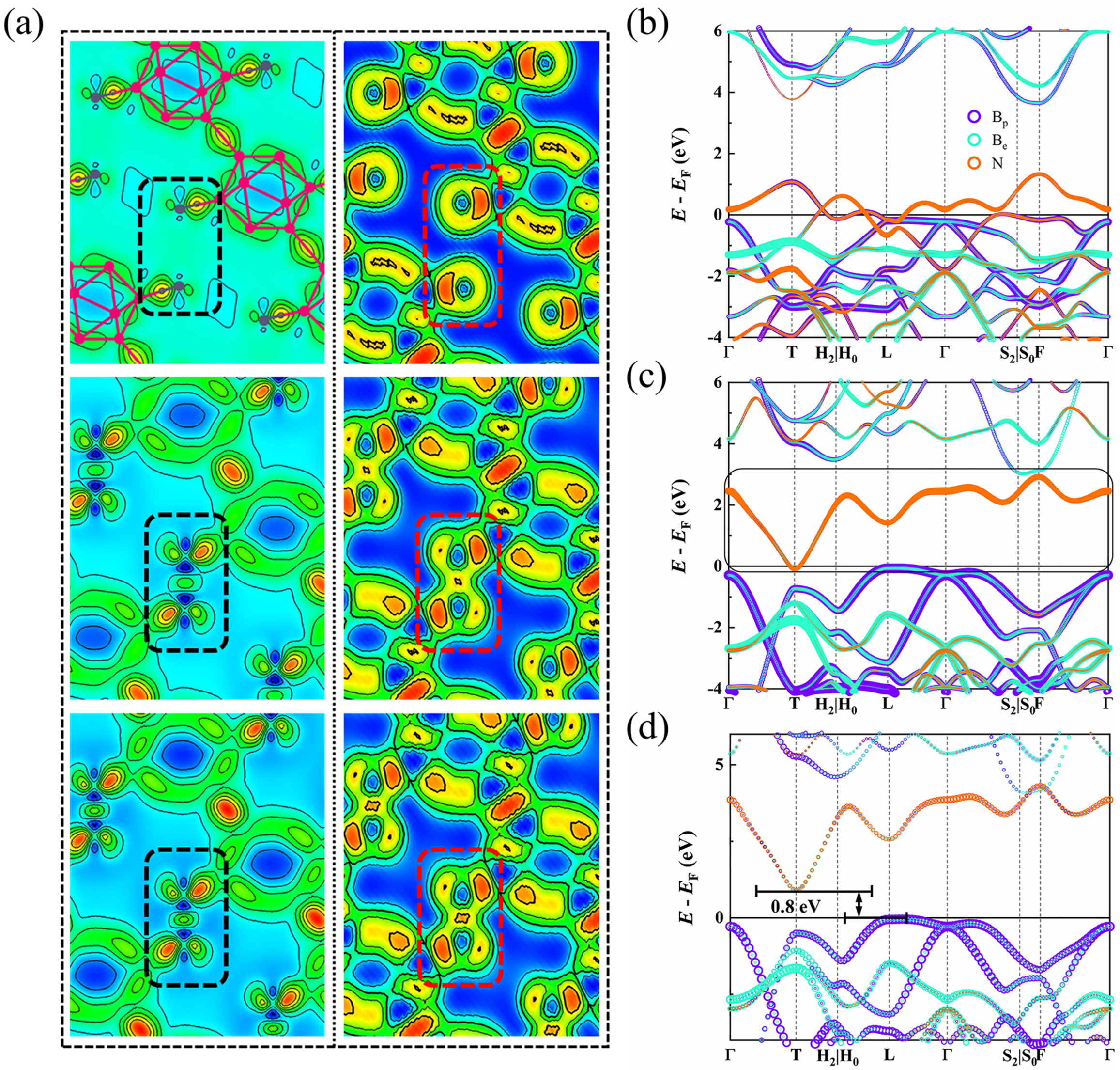

FIG. 3. (a) VCDD (left panel) and ELF (right panel) of $R\bar{3}m$ B_6N at 0, 120, and 200 GPa (from top to bottom). Color scales for VCDD and ELF run from −0.05 to 0.1 and 0 to 1, respectively. Band structures of $R\bar{3}m$ B_6N at (b) 0 GPa, (c) 120 GPa (GGA), and (d) 120 GPa (HSE).

and N atoms (see the partially occupied bands across the Fermi level) (Figs. 3(b) and S6(b) [42]). When the pressure increases to 120 GPa, individual N-contributing bands appear above the Fermi level (black rectangles in Figs. 3(c) and S6(c) [42]), which results in the separation between the conduction and valence bands. These band structures were also confirmed by the calculations using the hybrid functional method (HSE06) [54], which exhibits a semiconductor feature with a band gap of ∼0.8 eV for $R\bar{3}m$ B_6N [Fig. 3(d)] and ∼1.3 eV for *Cmcm* B_6N (Fig. S6(d) [42]), verifying a metal-semiconductor transition (MST). Figure S7 [42] shows that both GGA and HSE reveal this transition in the same manner but only the former underestimates the band gap. Hence in the following discussion, we will focus on the GGA results.

By analyzing the crystal orbital Hamilton population (COHP) of B_p–B_p, B_e–N, and N-N bonds, the correlation between the orbital pattern with this unprecedented isopointal MST is obtained for $R\bar{3}m$ B_6N. At zero pressure, an eye-catching bonding state across the Fermi level can be observed in the B_p–B_p bond [red arrow in Fig. 4(a)], which corresponds to the small spindle-shaped charge confirmed by the partial charge density (PCD) [red arrowheads in Fig. 4(c)], indicating its partially occupied feature, while for the N-N bond, neither bonding nor antibonding fingerprints can be found because of its nonbonding nature. However, the calculated orbital-resolved density of states (DOS) clearly shows a large electronic state around the Fermi level that arises from the N atoms (blue arrow). The associated orbital pattern [blue arrowheads in Fig. 4(c)] reveals that such electronic states represent the distribution of the lone pair electrons lying in the $2p_z$ orbital which stems from the sp^2-like hybridizations of the N atoms, evidenced by the detailed orbital-resolved DOS (Fig. S8 [42]) and the slightly disturbed planar configuration possessed by three equivalent B_e–N bonds (bond angle is ∼118.7°). After the phase transition at 120 GPa, a pronounced bonding state can be observed in the N-N bond as expected [the corresponding bond strength (-ICOHP) is ∼6.53] [Fig. 4(b)]. Accordingly, a σ^* antibonding state [blue arrowheads in Fig. 4(d)] appears above the Fermi level, where the original lone pair electrons participate in N-N bonding.

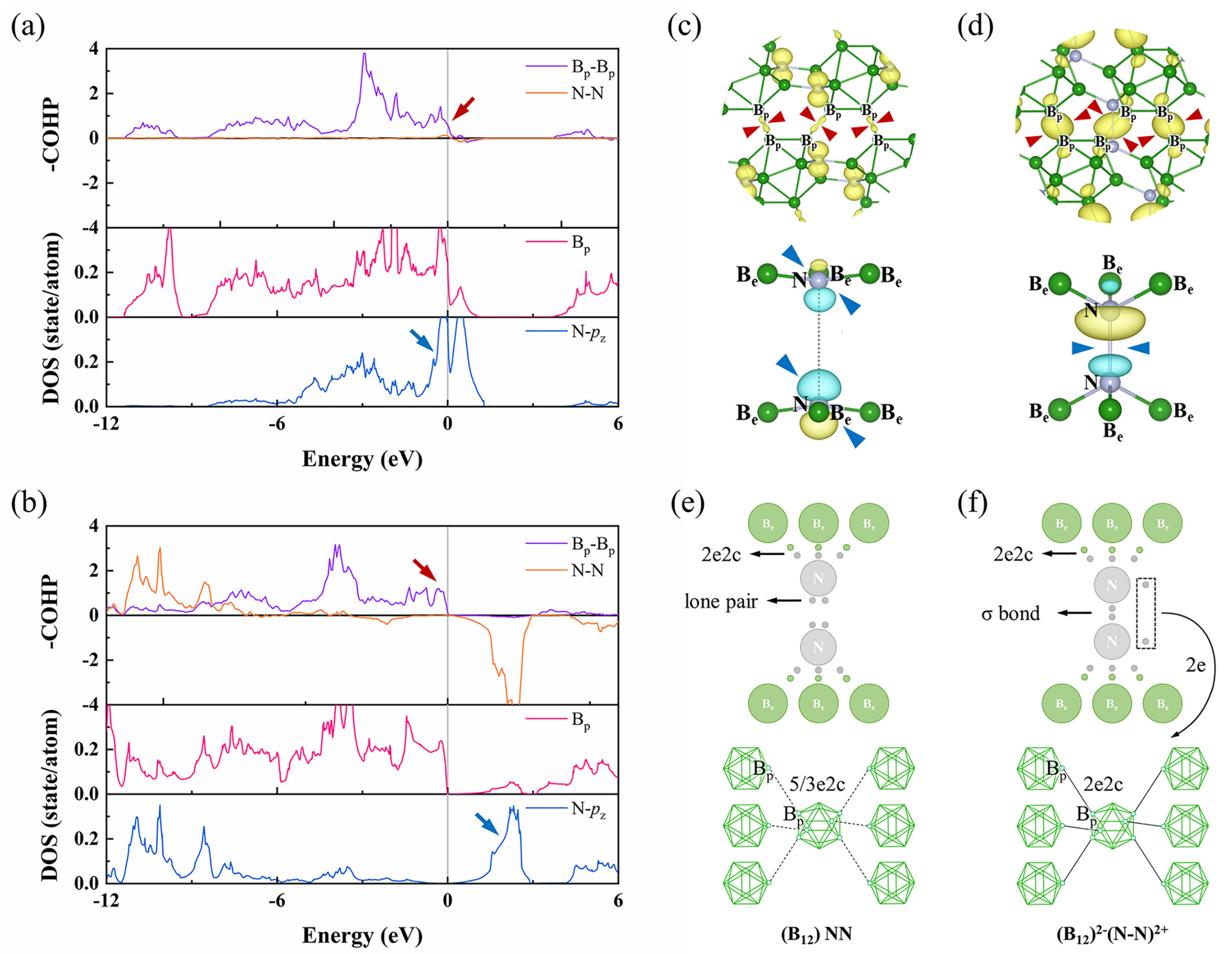

FIG. 4. COHP curves of $B_p{-}B_p$ and N-N bonds in $R\bar{3}m$ B_6N and the associated DOS at (a) 0 GPa and (b) 120 GPa. PCD and lone pair states derived from (c) partially occupied bands that cross the Fermi level at 0 GPa and (d) VBM and CBM at 120 GPa. The same PCD isosurface 0.013 is adopted. (e), (f) Schematic representation of the electron occupation changes from 0 to 120 GPa, where the upper and lower parts show the bonding orbitals related to the N-N and $B_p{-}B_p$ bonds, respectively, and the electrons are color coded to match the atoms that donated them.

Meanwhile, the partial filling bonding states of the $B_p{-}B_p$ bond are being fully filled (red arrow), corresponding to the large charge accumulation regions in the PCD of the valence band maximum (VBM) [red arrowheads in Fig. 4(d)]. In contrast, the $B_e{-}N$ bond is rarely affected by pressure with a negligible increase of -ICOHP ~0.02, and remains the strongest bonding unit. Very similar results are also observed in *Cmcm* B_6N, except that the lone pairs present in the $2p_y$ orbitals (Fig. S9 [42]). It is noteworthy that the MST observed in boron subnitride is highly unusual because in other icosahedral borides, the electronic behavior under pressure can be attributed to the bandwidth changes dominated by the CBM states [76] (Fig. S10 [42]) rather than the repopulation of local bonding orbitals.

In combination with the established bonding characters that have achieved success in explaining the physical properties of icosahedral borides [77–81], taking $R\bar{3}m$ B_6N as an example, we assigned a simplified electron counting scheme to understand such transition [Figs. 4(e) and 4(f)]. Recall that 26 of 36 valence electrons provided by the B_{12} icosahedron must occupy the 13 intraicosahedral bonding orbitals to satisfy Wade's rule (i.e., to stabilize the B_{12} skeleton [29,82]), which leaves only ten electrons to fill the 12 external bonding orbitals [six bonds between polar B (B_p) atoms and six bonds between equatorial B (B_e) atoms and chain atoms], resulting in an electron deficiency of 2. In α-B_{12}, such electron deficiency is resolved by forming a pair of two-electron three-center ($2e3c$) bonds among the six equatorial atoms [83], while in icosahedral compounds, the atomic chains running along the rhombohedral cell axis play an essential role in balancing such electron deficiency, depending on the numbers of electrons needed for intrachains [30,80,81,84]. For $R\bar{3}m$ B_6N at zero pressure, three of the five valence electrons of each N atom are utilized to fulfill six $B_e{-}N$ bonding orbitals. Because of the $2e$ deficiency, each six $B_p{-}B_p$ bond exhibits a partially filled $5/3e2c$ bond, And the nonbonding nature between N atoms makes the remaining two electrons placed as lone pairs but provides no additional electrons, forcing the $R\bar{3}m$ B_6N to

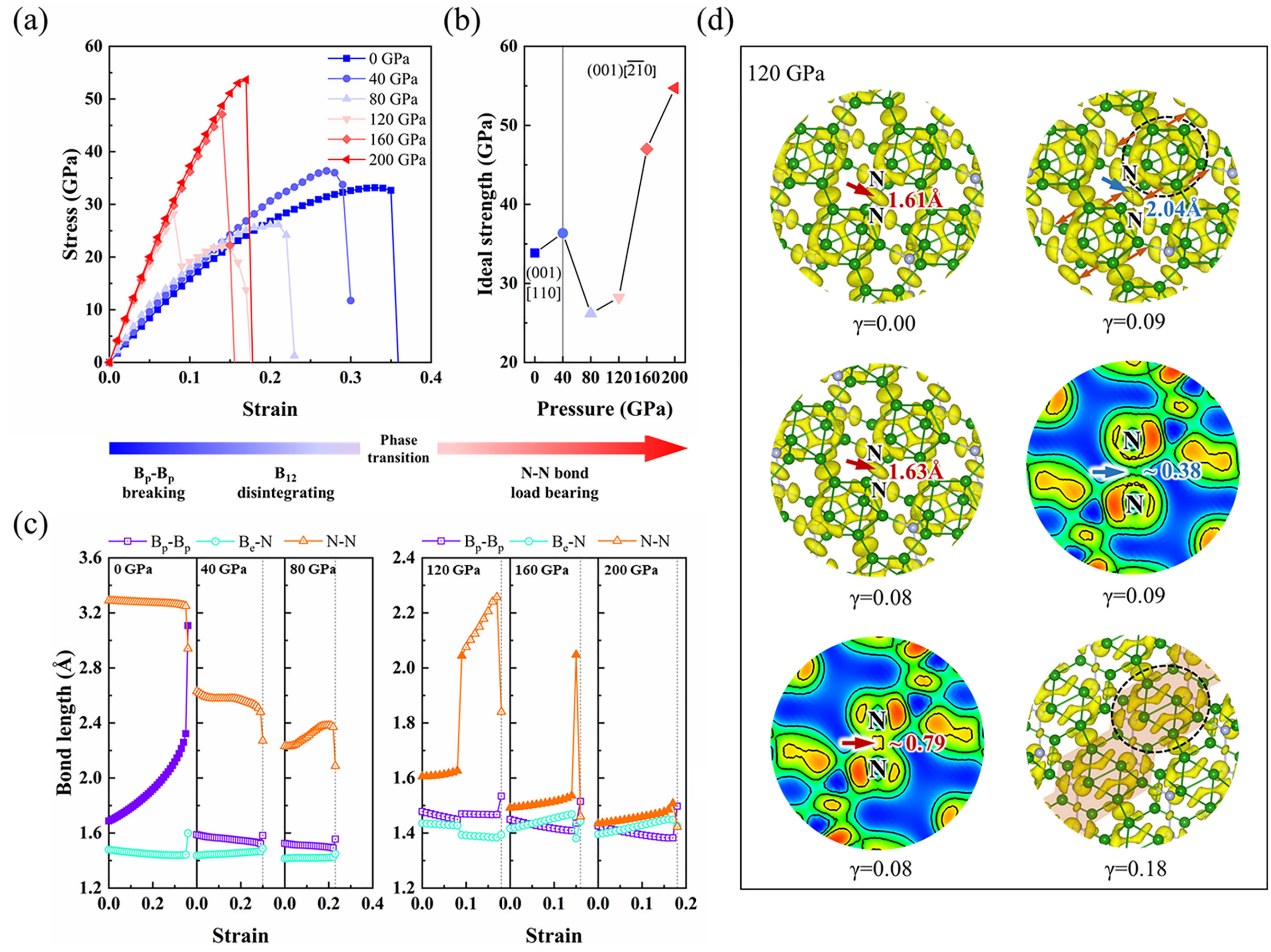

FIG. 5. (a) Stress-strain relationships, (b) corresponding ideal strength, and (c) key bond length variations of $R\bar{3}m$ B_6N at different pressures. (d) Calculated ELF isosurfaces (at 0.80) of deformed structures at key strains under 120 GPa. Two-dimensional slices regarding the N-N bond are also presented, for which the color scale runs from 0 to 1. The solid dots and vertical dotted lines in (c) represent the main load-bearing component in the corresponding strain range and the failure strain caused by the disintegration of the B_{12} unit, respectively. The collapse of the B_{12} unit is highlighted as black dashed circles, light orange arrows, and areas in (d).

behave as being electron deficient and thus metallically conductive. When the pressure increases to 120 GPa, the $(N\text{-}N)^{2+}$ dumbbell forms, and breaks the lone pairs and leaves a surplus of one electron for each N atom. Consequently, the partially filled B_p-B_p bonding orbitals become fully occupied through the compensation by these two electrons, eventually becoming an electron-precise $B_{12}^{2-}(N\text{-}N)^{2+}$ with semiconducting properties. Note that the chain atoms contributing electrons to the B_p-B_p bond were also observed in $B_{13}C_2$ [80,85]. The occurrence of this charge transfer also provides direct proof for the predicted change of electronegativities under pressure [86].

To elucidate the effect of MST on the mechanical behaviors of $R\bar{3}m$ B_6N and *Cmcm* B_6N, we first calculated their elastic moduli under pressure and compared them with other B_{12}-based compounds. As shown in Fig. S11(a) [42], MST leads to an obvious increase in the bulk modulus of B_6N, which finally exceeds that of B_6O at higher pressures. More strikingly, the shear modulus of B_6N continues to increase with pressure, exceeding B_6O by ∼65% at 120 GPa and even reaching 390 GPa at 200 GPa (Fig. S11(b) [42]), almost twice as high as the latter. These sharp increases of modulus correspond to the rapid decrease of the N-N bond distance (Fig. S11(c) [42]). The orientational features of shear modulus shown in Fig. S11(d) [42] show that B_6N exhibits a more isotropic feature than B_6O at 120 GPa, whereas the latter shows extreme directional dependence. This can be attributed to a more average spatial electron density [87] resulting from the MST, i.e., a simultaneous stiffening of the N-N bond, B_{12} unit, and B_p-B_p bond, in contrast with the localized electron densification and bond stiffening in B_6O without O-O bonding.

We next turn to the atomistic understanding of the deformation mechanisms of boron subnitride under large strains, obtained by imposing shear strain along their possible slip systems at different pressures (Figs. S12 and S13 [42]). The stress-strain relationships along the weakest shear path and the corresponding ideal strength, which are highly correlated to the realistic plastic behavior of the B_{12} compounds [6,73,88–90], are summarized in Figs. 5(a) and 5(b). For

$R\bar{3}m$ B_6N, the (001)[110] slip system has the lowest shear strength of 33.7 GPa under a critical strain of 0.33 at zero pressure. The bond length variations [Fig. 5(c)] show that the $B_p\text{—}B_p$ bond continues to weaken and the stress drops abruptly after it is broken (as illustrated by the complete disappearance of localized electrons in Fig. S14 [42]), indicating the $B_p\text{—}B_p$ bond is the main load-bearing component. As the pressure increases from 0 to 40 and then to 80 GPa, $R\bar{3}m$ B_6N undergoes a process from a slight strengthening to a sudden softening due to the changes in the weakest slip system and the associated load-bearing units (Fig. S14 [42]). When the pressure reaches 120 GPa (i.e., MST pressure), the stress response exhibits an intriguing creeplike deformation mode [87,88,91], where a second response regime appears from the strain of 0.90–0.14 after the peak-to-valley drop. This unusual behavior stems from a sequential bond breaking process. As shown by the bond length and ELF changes [Fig. 5(d)], the formation of the N-N bond at this pressure allows it to bear the loadings and dominates the first stage of the rapid stress growth (up to a strain of 0.08). After the stress release by the breaking of N-N bonds (the corresponding ELF value decreases drastically from ~0.79 to ~0.38), the B_{12} unit becomes the main load-bearing component, producing the second response regime until it disintegrates [see black dashed circles in Fig. 5(d), where the complete charge network used to stabilize the B_{12} skeleton is broken]. The deformation behavior at 200 GPa exhibits a similar pattern to that at 160 GPa (Fig. S14 [42]), where the N-N bond strength becomes very close to that of the strongest $B_e\text{—}N$ bond (the -ICOHP difference is only ~0.72), thus achieving a significant enhancement in strength (54.2 GPa) that is comparable to that of B_6O (57.5 GPa) (Fig. S15(a) [42]). It is worth noting that although B_6P has the shortest chain bond among these B_{12}-based borides, its P-P bond is rarely affected by pressure (Fig. S11(c) [42]). The weak P-P bond does not contribute to resist plastic strain at high pressures, and thus leads to very low strength (e.g., 22.5 GPa at 200 GPa) (Fig. S15(b) [42]). Owing to the comparable bonding situations, *Cmcm* B_6N possesses similar deformation behaviors (Figs. S16 and S17 [42]) to $R\bar{3}m$ B_6N. In brief, the extraordinary MST-driven stiffening is attributed to the complex competition between different structural fragments, where various bonding units in boron subnitride exhibit a distinct mechanical response, resulting in different strengths and failure strains. This goes beyond the previous studies on a few boron-rich compounds at ambient pressure condition [11,73,81,88], offering fresh insights into a broader class of covalent crystals with complex bonding networks.

In summary, we identified the realistic crystal structure of the long-debated boron subnitride as $R\bar{3}m$ B_6N and elucidated the electronic origin for its experimentally observed unique metallic feature. The isopointal MST was revealed by the local orbital population coupling between different homonuclear bonds under high pressure. At 120 GPa, the breakage of the lone pairs lying in the N-$2p_z$ orbital resulting from the formation of a $(\text{N-N})^{2+}$ dumbbell compensates for the unoccupied bonding states of the intericosahedra B-B bonds, thus turning it into an electron-precise $B_{12}^{2-}(\text{N-N})^{2+}$. The MST leads to the ultrastiffening of boron subnitride, where the N-N bond grants it the highest modulus among B_{12}-based compounds and plays a dominant role in its exceptional strength. These findings broaden the in-depth understanding of the boron-based compound, and contribute to a comprehensive grasp of chemical pattern modifications under high pressures.

The authors acknowledge the National Natural Science Foundation of China (NSFC), Grant No. 51672015, the National Key Research and Development Program of China (Grant No. 2017YFB0702100), the "111 Project" (Project No. B17002), the National Thousand Young Talents Program of China, and Fundamental Research Funds for the Central Universities. D.L. acknowledges the support from Czech Science Foundation Project No. 23-07228S, and support from Ministry of Education, Youth and Sports of the Czech Republic by OP JAK Project No. CZ.02.01.01/00/22_008/0004572 and project e-INFRA CZ (ID:90254). The authors also thank Dr. Shihao Zhang and Dr. Zhongheng Fu for their helpful discussions.

---

[1] B. Albert and H. Hillebrecht, Boron: Elementary challenge for experimenters and theoreticians, Angew. Chem. Int. Ed. Engl. **48**, 8640 (2009).

[2] X.-F. Zhou, X. Dong, A. R. Oganov, Q. Zhu, Y. J. Tian, and H. T. Wang, Semimetallic two-dimensional boron allotrope with massless Dirac fermions, Phys. Rev. Lett. **112**, 085502 (2014).

[3] E. Y. Zarechnaya, L. Dubrovinsky, N. Dubrovinskaia, Y. Filinchuk, D. Chernyshov, V. Dmitriev, N. Miyajima, A. El Goresy, H. F. Braun, S. Van Smaalen *et al.*, Superhard semiconducting optically transparent high pressure phase of boron, Phys. Rev. Lett. **102**, 185501 (2009).

[4] T. Ogitsu, E. Schwegler, and G. Galli, β-Rhombohedral boron: At the crossroads of the chemistry of boron and the physics of frustration, Chem. Rev. **113**, 3425 (2013).

[5] V. Domnich, S. Reynaud, R. A. Haber, and M. Chhowalla, Boron carbide: Structure, properties, and stability under stress, J. Am. Ceram. Soc. **94**, 3605 (2011).

[6] Q. An, W. A. Goddard III, K. Y. Xie, G. D. Sim, K. J. Hemker, T. Munhollon, M. F. Toksoy, and R. A. Haber, Superstrength through nanotwinning, Nano Lett. **16**, 7573 (2016).

[7] K. Y. Xie, Q. An, T. Sato, A. J. Breen, S. P. Ringer, W. A. Goddard III, J. M. Cairney, and K. J. Hemker, Breaking the icosahedra in boron carbide, Proc. Natl. Acad. Sci. USA **113**, 12012 (2016).

[8] K. Rasim, R. Ramlau, A. Leithe-Jasper, T. Mori, U. Burkhardt, H. Borrmann, W. Schnelle, C. Carbogno, M. Scheffler, and Y. Grin, Local atomic arrangements and band structure of boron carbide, Angew. Chem. Int. Ed. **57**, 6130 (2018).

[9] A. Jay, O. H. Duparc, J. Sjakste, and N. Vast, Theoretical Raman spectrum of boron carbide $B_{4.3}C$ under pressure, Acta Mater. **255**, 119085 (2023).

[10] D. He, Y. Zhao, L. Daemen, J. Qian, T. D. Shen, and T. W. Zerda, Boron suboxide: As hard as cubic boron nitride, Appl. Phys. Lett. **81**, 643 (2002).

[11] R. F. Zhang, Z. J. Lin, Y. S. Zhao, and S. Veprek, Superhard materials with low elastic moduli: Three-dimensional covalent bonding as the origin of superhardness in B_6O, Phys. Rev. B **83**, 092101 (2011).

[12] C. Kunka, X. Yang, Q. An, and G. Subhash, Icosahedral superstrength at the nanoscale, Phys. Rev. Mater. **2**, 063606 (2018).

[13] D. Emin, Unusual properties of icosahedral boron-rich solids, J. Solid State Chem. **179**, 2791 (2006).

[14] K. Shirai, Electronic structures and mechanical properties of boron and boron-rich crystals (Part I), J. Superhard Mater. **32**, 205 (2010).

[15] A. Ektarawong, S. I. Simak, and B. Alling, Structural models of increasing complexity for icosahedral boron carbide with compositions throughout the single-phase region from first principles, Phys. Rev. B **97**, 174104 (2018).

[16] T. Mori, Thermoelectric and magnetic properties of rare earth borides: Boron cluster and layered compounds, J. Solid State Chem. **275**, 70 (2019).

[17] H. Werheit, B. Herstell, W. Winkelbauer, G. Pristáš, S. Gabáni, K. Flachbart, and S. Shalamberidze, Electrical conductivity of boron carbide from ∼5 to ∼2100 K in the whole homogeneity range, Solid State Sci. **132**, 106987 (2022).

[18] H. Hubert, L. A. Garvie, P. R. Buseck, W. T. Petuskey, and P. F. McMillan, High-pressure, high-temperature syntheses in the B-C-N-O system, J. Solid State Chem. **133**, 356 (1997).

[19] L. A. Garvie, H. Hubert, W. T. Petuskey, P. F. McMillan, and P. R. Buseck, High-pressure, high-temperature syntheses in the B-C-N-O system, J. Solid State Chem. **133**, 365 (1997).

[20] A. Ektarawong, S. I. Simak, and B. Alling, Thermodynamic stability and properties of boron subnitrides from first principles, Phys. Rev. B **95**, 064206 (2017).

[21] V. L. Solozhenko and O. O. Kurakevych, New boron subnitride $B_{13}N_2$: HP-HT synthesis, structure and equation of state, J. Phys.: Conf. Ser. **121**, 062001 (2008).

[22] P. F. McMillan, New materials from high-pressure experiments, Nat. Mater. **1**, 19 (2002).

[23] A. R. Oganov, J. Chen, C. Gatti, Y. Ma, C. Glass, Z. Liu, T. Yu, O. Kurakevych, and V. Solozhenko, Ionic high-pressure form of elemental boron, Nature (London) **457**, 863 (2009).

[24] F. Peng, M. S. Miao, H. Wang, Q. Li, and Y. M. Ma, Predicted lithium-boron compounds under high pressure, J. Am. Chem. Soc. **134**, 18599 (2012).

[25] I. Harran, Y. Z. Chen, H. Y. Wang, and Y. X. Ni, Pressure induced evolution of structures and properties of iron tetraboride, CrystEngComm **20**, 3928 (2018).

[26] Y. Zhang, W. Wu, Y. Wang, S. A. Yang, and Y. Ma, Pressure-stabilized semiconducting electrides in alkaline-earth-metal subnitrides, J. Am. Chem. Soc. **139**, 13798 (2017).

[27] M. Bykov, E. Bykova, G. Aprilis, K. Glazyrin, E. Koemets, I. Chuvashova, I. Kupenko, C. McCammon, M. Mezouar, V. Prakapenka *et al.*, Fe-N system at high pressure reveals a compound featuring polymeric nitrogen chains, Nat. Commun. **9**, 2756 (2018).

[28] D. Laniel, B. Winkler, E. Koemets, T. Fedotenko, M. Bykov, E. Bykova, L. Dubrovinsky, and N. Dubrovinskaia, Synthesis of magnesium-nitrogen salts of polynitrogen anions, Nat. Commun. **10**, 4515 (2019).

[29] M. Miao, Y. Sun, E. Zurek, and H. Lin, Chemistry under high pressure, Nat. Rev. Chem. **4**, 508 (2020).

[30] H. Zhang, S. Yao, and M. Widom, Predicted phase diagram of boron-carbon-nitrogen, Phys. Rev. B **93**, 144107 (2016).

[31] G. A. Slack, T. F. McNelly, and E. A. Taft, Melt growth and properties of B_6P crystals, J. Phys. Chem. Solids **44**, 1009 (1983).

[32] G. A. Slack and K. E. Morgan, Some crystallography, chemistry, physics, and thermodynamics of $B_{12}O_2$, $B_{12}P_2$, $B_{12}As_2$, and related alpha-boron type crystals, J. Phys. Chem. Solids **75**, 1054 (2014).

[33] J. Z. Wu, H. Y. Zhu, D. B. Hou, C. G. Ji, C. E. Whiteley, J. H. Edgar, and Y. Z. Ma, High pressure x-ray diffraction study on icosahedral boron arsenide ($B_{12}As_2$), J. Phys. Chem. Solids **72**, 144 (2011).

[34] H. Dong, A. R. Oganov, V. V. Brazhkin, Q. Wang, J. Zhang, M. M. Davari Esfahani, X.-F. Zhou, F. Wu, and Q. Zhu, Boron oxides under pressure: Prediction of the hardest oxides, Phys. Rev. B **98**, 174109 (2018).

[35] Y. Wang, Y. Wang, T. Yao, H. Li, L. Wu, M. Yang, J. Zhang, and H. Gou, Metallization and softening of B_6O at high pressure, J. Alloys Compd. **600**, 71 (2014).

[36] K. Shirai, H. Dekura, and A. Yanase, Electronic structure and electrical resistivity of α-boron under high pressure, J. Phys. Soc. Jpn. **78**, 084714 (2009).

[37] J. Zhao and J. P. Lu, Pressure-induced metallization in solid boron, Phys. Rev. B **66**, 092101 (2002).

[38] S. Aryal, P. Rulis, and W. Y. Ching, Mechanism for amorphization of boron carbide B_4C under uniaxial compression, Phys. Rev. B **84**, 184112 (2011).

[39] A. P. Awasthi and G. Subhash, High-pressure deformation and amorphization in boron carbide, J. Appl. Phys. **125**, 215901 (2019).

[40] Y. P. Lu and D. W. He, Structure and elastic properties of boron suboxide at 240 GPa, J. Appl. Phys. **105**, 083540 (2009).

[41] L. Wang, R. Sun, W. Liu, Z. Yuan, A. Bergara, X. Liang, S. Chen, X. Zhou, B. Xu, J. He *et al.*, Novel superhard boron-rich nitrides under pressure, Sci. China Mater. **63**, 2358 (2020).

[42] See Supplemental Material at http://link.aps.org/supplemental/10.1103/PhysRevB.108.L180103 for more details on the methods used in this study, the crystal structures information, additional figures and tables, and the possible formation mechanism of $R\bar{3}m$ B_6N, which also includes Refs. [4,18,29,43–71].

[43] G. Kresse and J. Furthmüller, Efficient iterative schemes for *ab initio* total-energy calculations using a plane-wave basis set, Phys. Rev. B **54**, 11169 (1996).

[44] G. Kresse and D. Joubert, From ultrasoft pseudopotentials to the projector augmented-wave method, Phys. Rev. B **59**, 1758 (1999).

[45] J. P. Perdew, K. Burke, and M. Ernzerhof, Generalized gradient approximation made simple, Phys. Rev. Lett. **77**, 3865 (1996).

[46] M. Methfessel and A. T. Paxton, High-precision sampling for Brillouin-zone integration in metals, Phys. Rev. B **40**, 3616 (1989).

[47] H. J. Monkhorst and J. D. Pack, Special points for Brillouin-zone integrations, Phys. Rev. B **13**, 5188 (1976).

[48] S. Baroni, S. De Gironcoli, A. Dal Corso, and P. Giannozzi, Phonons and related crystal properties from density-functional perturbation theory, Rev. Mod. Phys. **73**, 515 (2001).

[49] A. Togo and I. Tanaka, First principles phonon calculations in materials science, Scr. Mater. **108**, 1 (2015).

[50] S. Maintz, V. L. Deringer, A. L. Tchougréeff, and R. Dronskowski, LOBSTER: A tool to extract chemical bonding from plane-wave based DFT, J. Comput. Chem. **37**, 1030 (2016).
[51] R. Nelson, C. Ertural, J. George, V. L. Deringer, G. Hautier, and R. Dronskowski, LOBSTER: Local orbital projections, atomic charges, and chemical-bonding analysis from projector-augmented-wave-based density-functional theory, J. Comput. Chem. **41**, 1931 (2020).
[52] R. Dronskowski and P. E. Blöchl, Crystal orbital Hamilton populations (COHP): Energy-resolved visualization of chemical bonding in solids based on density-functional calculations, J. Phys. Chem. C **97**, 8617 (1993).
[53] V. L. Deringer, A. L. Tchougréeff, and R. Dronskowski, Crystal orbital Hamilton population (COHP) analysis as projected from plane-wave basis sets, J. Phys. Chem. A **115**, 5461 (2011).
[54] J. Heyd, G. E. Scuseria, and M. Ernzerhof, Hybrid functionals based on a screened Coulomb potential, J. Chem. Phys. **118**, 8207 (2003).
[55] C. W. Glass, A. R. Oganov, and N. Hansen, USPEX-Evolutionary crystal structure prediction, Comput. Phys. Commun. **175**, 713 (2006).
[56] D. C. Lonie and E. Zurek, XTALOPT: An open-source evolutionary algorithm for crystal structure prediction, Comput. Phys. Commun. **182**, 372 (2011).
[57] Z. L. Liu, MUSE: Multi-algorithm collaborative crystal structure prediction, Comput. Phys. Commun. **185**, 1893 (2014).
[58] S. H. Zhang and R. F. Zhang, AELAS: Automatic ELAStic property derivations via high-throughput first-principles computation, Comput. Phys. Commun. **220**, 403 (2017).
[59] D. Roundy and M. L. Cohen, Ideal strength of diamond, Si, and Ge, Phys. Rev. B **64**, 212103 (2001).
[60] R. F. Zhang, S. H. Zhang, Y. Q. Guo, Z. H. Fu, D. Legut, T. C. Germann, and S. Veprek, First-principles design of strong solids: Approaches and applications, Phys. Rep. **826**, 1 (2019).
[61] S. H. Zhang, Z. H. Fu, and R. F. Zhang, ADAIS: Automatic derivation of anisotropic ideal strength via high-throughput first-principles computations, Comput. Phys. Commun. **238**, 244 (2019).
[62] S. H. Zhang, D. Legut, T. C. Germann, S. Veprek, H. J. Zhang, and R. F. Zhang, Plastic flow between nanometer-spaced planar defects in nanostructured diamond and boron nitride, Phys. Rev. B **101**, 014104 (2020).
[63] T. Xu, Z. Liu, D. Legut, and R. Zhang, Anomalous bond softening mediated by strain-induced Friedel-like oscillations in a BC_2N superlattice, Phys. Rev. B **106**, L060101 (2022).
[64] Z. H. Fu, Q. F. Zhang, D. Legut, C. Si, T. C. Germann, T. Lookman, S. Y. Du, J. S. Francisco, and R. F. Zhang, Stabilization and strengthening effects of functional groups in two-dimensional titanium carbide, Phys. Rev. B **94**, 104103 (2016).
[65] K. Momma and F. Izumi, VESTA 3 for three-dimensional visualization of crystal, volumetric and morphology data, J. Appl. Crystallogr. **44**, 1272 (2011).
[66] Z. R. Liu, B. N. Yao, and R. F. Zhang, SPaMD studio: An integrated platform for atomistic modeling, simulation, analysis, and visualization, Comput. Mater. Sci. **210**, 111027 (2021).
[67] X. Wang, Y. Wang, M. Miao, X. Zhong, J. Lv, T. Cui, J. Li, L. Chen, C. J. Pickard, and Y. Ma, Cagelike diamondoid nitrogen at high pressures, Phys. Rev. Lett. **109**, 175502 (2012).
[68] J. B. Condon, C. E. Holcombe, D. H. Johnson, and L. M. Steckel, The kinetics of the boron plus nitrogen reaction, Inorg. Chem. **15**, 2173 (1976).
[69] C. L. Perkins, M. Trenary, and T. Tanaka, Direct observation of $(B_{12})(B_{12})_{12}$ supericosahedra as the basic structural element in YB_{66}, Phys. Rev. Lett. **77**, 4772 (1996).
[70] H. Hubert, B. Devouard, L. A. Garvie, M. O'Keeffe, P. R. Buseck, W. T. Petuskey, and P. F. McMillan, Icosahedral packing of B_{12} icosahedra in boron suboxide (B_6O), Nature (London) **391**, 376 (1998).
[71] D. He, M. Akaishi, B. L. Scott, and Y. Zhao, Growth of boron suboxide crystals in the $B-B_2O_3$ system at high pressure and high temperature, J. Mater. Res. **17**, 284 (2002).
[72] Z.-J. Wu, E.-J. Zhao, H.-P. Xiang, X.-F. Hao, X.-J. Liu, and J. Meng, Crystal structures and elastic properties of superhard IrN_2 and IrN_3 from first principles, Phys. Rev. B **76**, 054115 (2007).
[73] Q. An, K. M. Reddy, H. Dong, M. W. Chen, A. R. Oganov, and W. A. Goddard III, Nanotwinned boron suboxide (B_6O): New ground state of B_6O, Nano Lett. **16**, 4236 (2016).
[74] H. Dong, A. R. Oganov, Q. Wang, S.-N. Wang, Z. Wang, J. Zhang, M. Mahdi Davari Esfahani, X.-F. Zhou, F. Wu, and Q. Zhu, Prediction of a new ground state of superhard compound B_6O at ambient conditions, Sci. Rep. **6**, 31288 (2016).
[75] Y. Wang, S. S. Wang, Y. Lu, J. Jiang, and S. A. Yang, Strain-induced isostructural and magnetic phase transitions in monolayer MoN_2, Nano Lett. **16**, 4576 (2016).
[76] H. Wang and Q. An, Band-gap engineering in high-temperature boron-rich icosahedral compounds, J. Phys. Chem. C **123**, 12505 (2019).
[77] M. M. Balakrishnarajan, P. D. Pancharatna, and R. Hoffmann, Structure and bonding in boron carbide: The invincibility of imperfections, New J. Chem. **31**, 473 (2007).
[78] H. C. Longuet-Higgins and M. D. V. Roberts, The electronic structure of an icosahedron of boron atoms, Proc. R. Soc. London, Ser. A **230**, 110 (1955).
[79] R. Hoffmann and W. N. Lipscomb, Theory of polyhedral molecules. I. physical factorizations of the secular equation, J. Chem. Phys. **36**, 2179 (1962).
[80] S. Mondal, Charge transfer and fractional bonds in stoichiometric boron carbide, Chem. Mater. **29**, 6191 (2017).
[81] Q. An and W. A. Goddard III, Boron suboxide and boron subphosphide crystals: Hard ceramics that shear without brittle failure, Chem. Mater. **27**, 2855 (2015).
[82] E. D. Jemmis, M. M. Balakrishnarajan, and P. D. Pancharatna, A unifying electron-counting rule for macropolyhedral boranes, metallaboranes, and metallocenes, J. Am. Chem. Soc. **123**, 4313 (2001).
[83] K. Wade, Structural and bonding patterns in cluster chemistry, Adv. Inorg. Chem. Radiochem. **18**, 1 (1976).
[84] S. Mondal, S. van Smaalen, G. Parakhonskiy, S. J. Prathapa, L. Noohinejad, E. Bykova, N. Dubrovinskaia, D. Chernyshov, and L. Dubrovinsky, Experimental evidence of orbital order in α-B_{12} and $\gamma-B_{28}$ polymorphs of elemental boron, Phys. Rev. B **88**, 024118 (2013).
[85] R. Schmechel, H. Werheit, T. U. Kampen, and W. Mönch, Photoluminescence of boron carbide, J. Solid State Chem. **177**, 566 (2004).

[86] M. Rahm, R. Cammi, N. W. Ashcroft, and R. Hoffmann, Squeezing all elements in the Periodic Table: Electron configuration and electronegativity of the atoms under compression, J. Am. Chem. Soc. **141**, 10253 (2019).

[87] H. Liang, H. Li, Q. Li, and C. Chen, Toughening a superstrong carbon crystal: Sequential bond-breaking mechanisms, Phys. Rev. B **102**, 134105 (2020).

[88] H. Liang, Q. Li, and C. Chen, Atomistic mechanisms for contrasting stress-strain relations of $B_{13}CN$ and $B_{13}C_2$, J. Phys. Chem. Lett. **11**, 10454 (2020).

[89] Q. An, W. A. Goddard III, and T. Cheng, Atomistic explanation of shear-induced amorphous band formation in boron carbide, Phys. Rev. Lett. **113**, 095501 (2014).

[90] Q. An, K. M. Reddy, J. Qian, K. J. Hemker, M. W. Chen, and W. A. Goddard III, Nucleation of amorphous shear bands at nanotwins in boron suboxide, Nat. Commun. **7**, 11001 (2016).

[91] M. Zhang, H. Liu, Q. Li, B. Gao, Y. Wang, H. Li, C. Chen, and Y. Ma, Superhard BC_3 in cubic diamond structure, Phys. Rev. Lett. **114**, 015502 (2015).